



Design of grain boundaries enriched nickel molybdate for enhanced catalytic oxidative desulfurization

Xin An^a, Wei Jiang^{a,b,*}, Linhua Zhu^b, Lingchao Xu^a, Junfeng She^a, Jing He^a, Wenshuai Zhu^{a,**}, Huaming Li^a

^a Institute for Energy Research and School of Chemistry and Chemical Engineering, Jiangsu University, Zhenjiang 212013, PR China

^b College of Chemistry and Chemical Engineering, Key Laboratory of Water Pollution Treatment and Resource Reuse of Hainan Province, Hainan Normal University, Haikou 571158, PR China

ARTICLE INFO

Keywords:

Oxidative desulfurization
Nickel molybdate
Grain boundaries
Oxygen vacancy
Electronic structure

ABSTRACT

Grain boundaries (GB), a favorable atomic configuration, can provide highly active surfaces by modulating electronic structures in the catalysts. Whereas, it is usually ignored owing to the large structural variations and the difficulty in its precise design. Herein, a novel strategy is proposed to prepare nickel molybdate with rich GB (RGB-NMO) via a facile one-step growth assisted by cetyltrimethylammonium bromide. Experimental results reveal that the optimized morphology can increase the exposure of active sites and facilitate the mass transfer during the oxidative desulfurization (ODS) reaction. Moreover, the engineered GB can modulate the surface atomic composition and electronic structure, leading to the increase of hydrogen peroxide activation capacity. Benefiting from these features, the synthesized RGB-NMO not only exhibits attractive desulfurization efficiency, but also shows a satisfactory cycling stability. Overall, this manuscript provides new inspirations for design of functional materials rich in GB towards excellent ODS treatment.

1. Introduction

The emission of SO_x is directly caused by sulfur-containing impurities in fuel oils, leading to a series of global environmental catastrophes, and even directly poses a threat to human property and health [1]. Therefore, the desulfurization of fuel has triggered worldwide interests with the purpose of reducing the damage to ecological environment [2, 3]. Meanwhile, the environment-related legislation has become increasingly stringent in China, and the sulfur content index of fuel oils may be limited to less than 10 ppm in the future [4,5]. Recently, hydrodesulfurization procedure, the main desulfurization technology in industry, requires harsh operation conditions such as high hydrogen pressure and high temperature [6–8]. However, the additional high energy consumption would undoubtedly contrary to the recent carbon neutrality policies. Therefore, adsorptive desulfurization, extractive desulfurization and oxidative desulfurization (ODS) as typical non-hydrogenation technologies have been developed to produce clean oil [9–11]. Among them, ODS technology, one of the most promising complementary methods, has attracted extensive attention owing to its

high removal efficiency of aromatic thiophenes and mild operation conditions [12–14].

The oxidant as an oxygen donor plays an essential role in the ODS procedure. Compared with cyclohexanone peroxide and tert-butyl hydroperoxide, hydrogen peroxide (H₂O₂) has been regarded as one of the most promising alternatives because of its specific merits such as less potential environmental issue, preferred economic cost and no hazardous by-product generation [15,16]. Whereas, H₂O₂ can only manifest high activity under the addition of an efficient catalyst during the ODS transformation [17–19]. Hence, seeking an appropriate catalyst for ODS has become the core issue at present [20,21].

Metal molybdates with the virtues of rich resources, environmental friendliness and low cost has been considered as scalable, effective and promising materials in catalytic reactions [22–24]. Particularly, utilization of nickel molybdate (NiMoO₄) as the catalyst shows advantages in terms of uniform distribution of active sites and multiple oxidation states, which makes it arouse extensive attention in various catalytic applications [25]. Besides, previous studies have reported that NiMoO₄ possessed a more stable structure and manifests higher catalytic

* Corresponding author at: Institute for Energy Research and School of Chemistry and Chemical Engineering, Jiangsu University, Zhenjiang 212013, PR China.

** Corresponding author.

E-mail addresses: jiangwei@ujs.edu.cn (W. Jiang), zhuws@ujs.edu.cn (W. Zhu).

performance relative to other transition metal molybdates [26–28]. However, its practical application into ODS is greatly restricted by the lack of accessible active centers for reaction. Therefore, developing an appropriate strategy to cope with this restriction to effectively enhance the catalytic ODS activity of NiMoO_4 is highly desired.

As is known, for catalytic reactions, regulating the surface electronic structure is of great importance to improve the catalytic activity, which is due to the fact that the atoms exposed on the surface of catalysts directly participate in the reaction. Recently, it is reported that defect engineering has been considered as an appealing method to enhance the catalytic activity [29,30]. Specifically, the defect structures such as disorders, pits, edge vacancies and vacancy pairs have been employed to significantly adjust electronic states neighboring the defects and atomic configurations, thus affecting the physicochemical properties [31–33]. Among them, grain boundary, a typical two-dimensional defect, plays a decisive role in modulating surface electron properties between various crystal planes, which features the satisfactory intrinsic catalytic activity induced by the refined local atomic arrangement of GB [34,35]. For example, Huang et al. [36] found that the GB of bimetallic borides $\text{Ni}_3\text{B}/\text{MoB}$ nanosheets can provide highly active surfaces by optimizing electronic structure of the catalyst, which leads to the enhanced catalytic HER activity. Although it has been reported that GB engineering has been employed to boost catalytic activity, the obstacles that large structural variations and the difficulty in precise design remarkably limit its potential practical application in the field of ODS transformation [37]. Therefore, it is desirable to deliberately design functional materials that can leverage the advantages of GB to improve the desulfurization performance.

Herein, an appealing method is proposed for GB engineering to increase the surface active sites via a CTAB-assisted hydrothermal synthesis strategy. NiMoO_4 with rich grain boundaries (RGB-NMO) was obtained by adding cetyltrimethylammonium bromide (CTAB) during the synthesis process. The results show that RGB-NMO has been illustrated to feature stronger hydrogen peroxide activation capacity, improving catalytic ODS activity relative to NiMoO_4 with lean GB (LGB-NMO), in which the sulfur removal for dibenzothiophene (DBT) can reach 100% by RGB-NMO within 30 min but only 41.6% by LGB-NMO. This phenomenon is caused by its adjusted electronic structure and surface atomic composition through GB engineering. Moreover, for RGB-NMO, the larger specific surface area can improve the exposure of active sites and facilitate the adsorption and desorption process during the ODS reaction. Besides, it also shows superior cycling stability and 96.9% of DBT could be removed after 14 cycles. This work would supply a facile strategy to prepare efficient catalysts enriched GB, thus generating sulfur-free fuels via ODS transformation.

2. Experimental section

2.1. Materials

Sodium molybdate dihydrate ($\text{Na}_2\text{MoO}_4 \cdot 2 \text{H}_2\text{O}$), nickel nitrate hexahydrate ($\text{Ni}(\text{NO}_3)_2 \cdot 6 \text{H}_2\text{O}$) and ethanol (AR) were bought from Sinopharm Chemical Reagent Co., Ltd. Dibenzothiophene (DBT, 98%), 4,6-dimethyldibenzothiophene (4,6-DMDBT, 97%) were purchased from Sigma-Aldrich. 4-Methyldibenzothiophene (4-MDBT, 96%), dodecane ($\text{C}_{12}\text{H}_{26}$, 98%) and hexadecane ($\text{C}_{16}\text{H}_{34}$, 98%) were bought from Aladdin Chemical. Cetyltrimethylammonium bromide (CTAB), tetradecyltrimethylammonium bromide (TTAB), dodecyl trimethyl ammonium bromide (DTAB), and tetramethylammonium bromide (TMAB) were bought from Shanghai Hushi. 1-Octyl-3-methylimidazolium tetrafluoroborate ([OMIM] BF_4) was bought from Shanghai Chengjie, and deionized water was purified by the laboratory.

2.2. Synthesis of catalysts

In this study, RGB-NMO was prepared by a hydrothermal synthesis.

First, 1 mmol of $\text{Na}_2\text{MoO}_4 \cdot 2 \text{H}_2\text{O}$ and 1 mmol of $\text{Ni}(\text{NO}_3)_2 \cdot 6 \text{H}_2\text{O}$ were mixed with 50 mL of deionized water. Following keep stirring vigorously for 1 h to form a light green solution. After that, a certain amount of CTAB (7.5 g/L) was dissolved into the above solution and further sonicated for 10 min to obtain a uniform suspension. Subsequently, the mixture was stirred for another 1 h to form the clear solution. And then, the solution was sealed in a Teflon liner (100 mL of capacity) and heated at 180 °C for 16 h. Finally, the resulting product was washed with deionized water and ethanol for 3 times, respectively, before drying in oven overnight. And the LGB-NMO was synthesized via the same method without the assistance of CTAB.

2.3. ODS of the model oil

The model oils were prepared by dissolving DBT, 4-MDBT and 4,6-DMDBT into dodecane with the sulfur content of 200 ppm, respectively. The typical ODS transformation was operated at 60 °C, 20 mg of catalyst, 1 mL of [OMIM] BF_4 and 5 mL of model oil were added into a customized double neck reactor with vigorous stirring. Extraction equilibrium was achieved by magnetic stirring for 10 min before adding 16 μL of H_2O_2 (30 wt%, the O/S ratio is 5) into the system. After the reaction, the sample was analyzed by gas chromatography to obtain the catalytic activity of prepared materials.

3. Results and discussion

3.1. Characterization of catalysts

LGB-NMO was prepared by a typical hydrothermal method of the mixture of molybdate dihydrate and nickel nitrate hexahydrate. As shown in Fig. 1a, the formed LGB-NMO nanorods with the length around 1.5 μm and a diameter around 0.2 μm were observed [38]. RGB-NMO was obtained through a same hydrothermal synthesis route with the addition of CTAB during the preparation process. It is observed that the blocky and platy morphology is generated via a CTAB-assisted strategy (Fig. 1b), which demonstrates that the presence of CTAB plays a vital role in the morphology of as-prepared samples. Besides, the transmission electron microscopy (TEM) images show that plentiful GB were built resulting from the alternative arrangement of three crystalline phases ($\text{NiMoO}_4 \cdot x\text{H}_2\text{O}$, $\alpha\text{-NiMoO}_4$ and $\beta\text{-NiMoO}_4$) in RGB-NMO after the introduction of CTAB (Fig. 1c and d). Specifically, the lattice fringe spacings of 0.27, 0.23 and 0.34 nm are contributed to $\text{NiMoO}_4 \cdot x\text{H}_2\text{O}$ (JCPDS No. 12–0348), $\alpha\text{-NiMoO}_4$ (JCPDS No. 33–0948) and $\beta\text{-NiMoO}_4$ (JCPDS No. 13–0128) crystal structures, respectively [39,40]. It is observed that the distortion and restructure in the fractional structure of RGB-NMO were generated, which is induced by sharing crystal edges to produce GB (Fig. 1d). In addition, the elemental mapping images are shown in Fig. S1, reflecting the uniform distribution of Mo, Ni and O elements in the RGB-NMO.

To explore the composition and structure of LGB-NMO and RGB-NMO, several characterizations were carried out. The X-ray diffraction (XRD) results show that the pattern of LGB-NMO is well indexed to the $\text{NiMoO}_4 \cdot x\text{H}_2\text{O}$ (JCPDS No. 12–0348) along with a little $\beta\text{-NiMoO}_4$ (JCPDS No. 13–0128) crystal phases (Fig. 2a) [27]. Compared with LGB-NMO, diffraction peaks of three crystalline phases ($\text{NiMoO}_4 \cdot x\text{H}_2\text{O}$, $\alpha\text{-NiMoO}_4$ and $\beta\text{-NiMoO}_4$) have been observed in RGB-NMO. Besides, the intensity of diffraction peaks located at 23.5° and 26.0° belonging to $\beta\text{-NiMoO}_4$ is higher than other diffraction peaks, suggesting that $\beta\text{-NiMoO}_4$ is main component in RGB-NMO. This phenomenon illustrates that this facile CTAB-assisted preparation strategy is in favor of the transformation from $\text{NiMoO}_4 \cdot x\text{H}_2\text{O}$ to $\alpha\text{-NiMoO}_4$ and $\beta\text{-NiMoO}_4$, thus facilitating the formation of extensive GB between them [41,42]. It is known that the obtained $\beta\text{-NiMoO}_4$ is found to be metastable β -phase, which features better catalytic activity than $\text{NiMoO}_4 \cdot x\text{H}_2\text{O}$ [43,44]. Meanwhile, the observed lower diffraction intensity means the lower crystallinity in RGB-NMO, which is consistent with the result of scanning

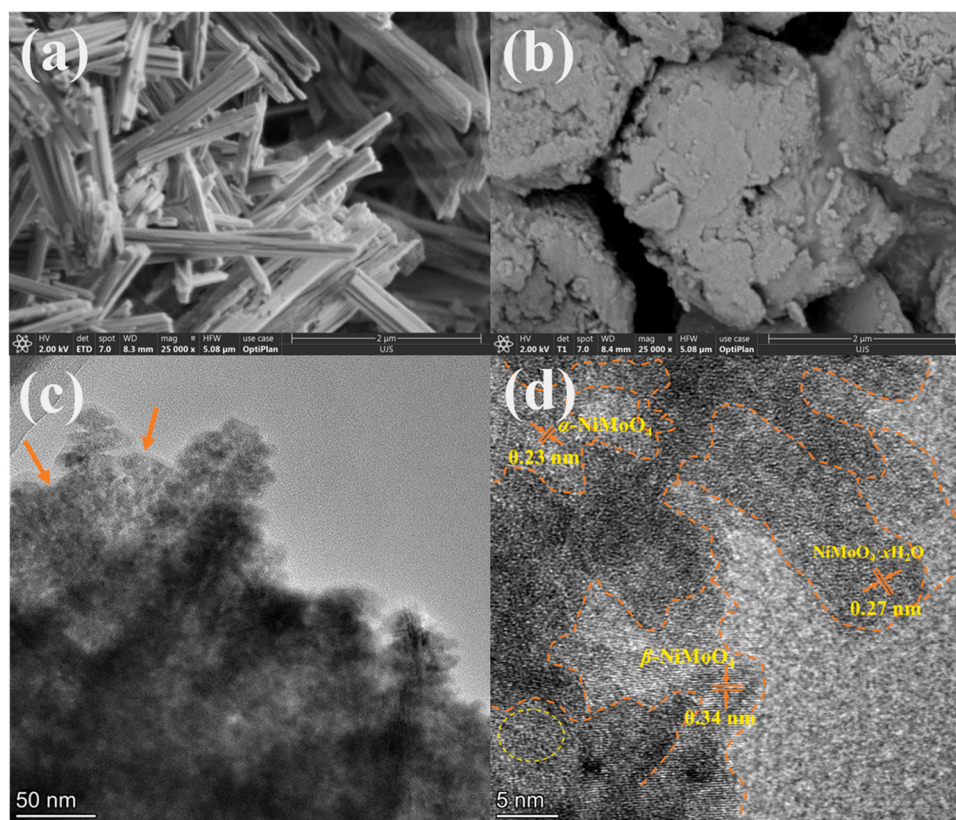


Fig. 1. SEM images of (a) LGB-NMO and (b) RGB-NMO. (c-d) HRTEM images of RGB-NMO.

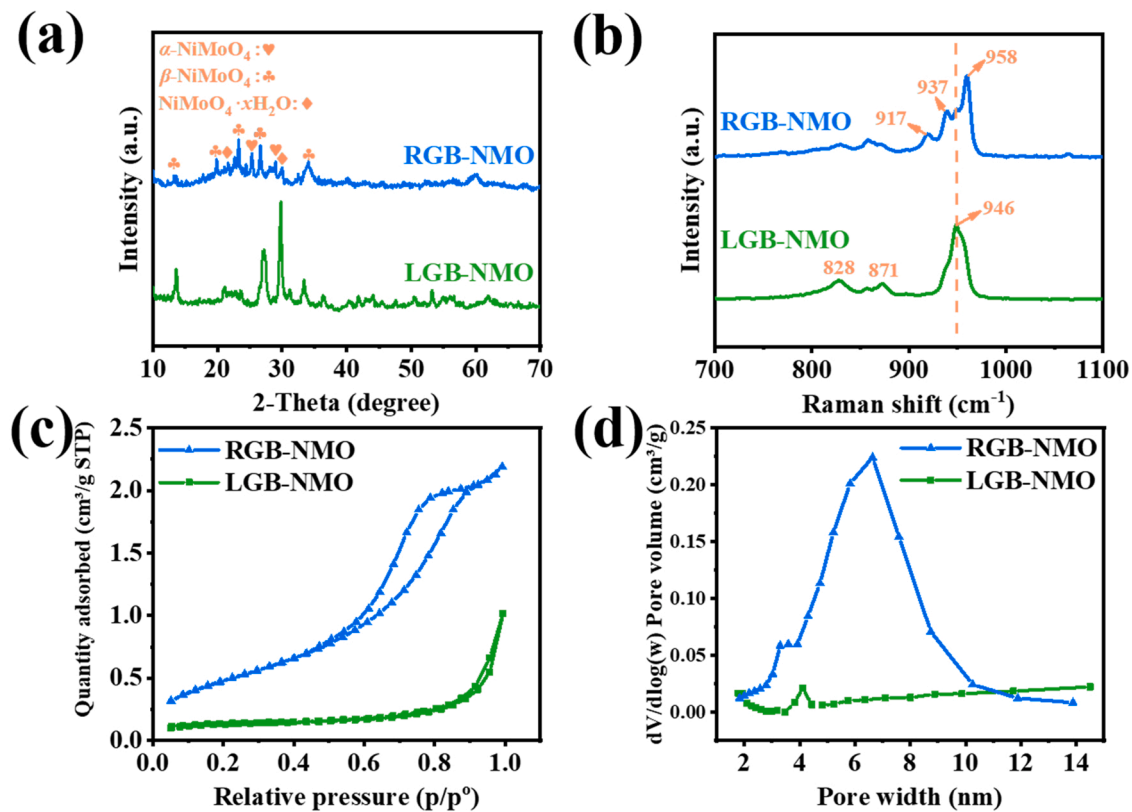


Fig. 2. (a) XRD, (b) Raman spectra, (c) N_2 adsorption-desorption isotherms and (d) the pore size distribution of LGB-NMO and RGB-NMO.

electron microscopy (SEM) analysis that the obtained RGB-NMO blocks are composed of the primary nanoparticles.

The microstructures of as-prepared materials were explored by the Fourier transform infrared (FT-IR) and Raman spectra. The FT-IR analysis of LGB-NMO shows that the main characteristic peaks at 741, 882 and 970 cm^{-1} are ascribed to the stretching vibration of Mo-O, Mo-O-Mo and Mo=O stretching modes (Fig. S2), respectively, which is attributed to $\text{NiMoO}_4 \cdot x\text{H}_2\text{O}$ phase [45,46]. It is noteworthy that the intensity of the peak located at 970 cm^{-1} is significantly decreased after introducing CTAB into synthesis process. Moreover, compared with LGB-NMO, a remarkable red shift of the peak corresponding to Mo-O (from 741 to 722 cm^{-1}) is also detected for the RGB-NMO. These phenomena may be caused by the transformation from $\text{NiMoO}_4 \cdot x\text{H}_2\text{O}$ to $\alpha\text{-NiMoO}_4$ and $\beta\text{-NiMoO}_4$. The Raman technique as a powerful tool is employed to further confirm this hypothesis. In the Raman spectrum of LGB-NMO, the strong peak around 946 cm^{-1} is resulted from the symmetric stretching of Mo=O bond (Fig. 2b). Other two weak peaks located at 828 and 871 cm^{-1} are assigned to the asymmetric M-O stretching mode, which belongs to the characteristics of $\text{NiMoO}_4 \cdot x\text{H}_2\text{O}$ [47,48]. Whereas, the strongest peak at 958 cm^{-1} along with the new peak at 917 cm^{-1} illustrates the formation of $\alpha\text{-NiMoO}_4$ [39]. And the observed peak located at 937 cm^{-1} originates from the MoO_4^{2-} ions symmetric stretch of $\beta\text{-NiMoO}_4$ [39]. According to above results, the remarkable microstructure difference between LGB-NMO and RGB-NMO further proves the formation of mixed crystalline phase, which is consistent with the result of XRD analysis.

The changes in the porosity between RGB-NMO and LGB-NMO were evaluated by N_2 adsorption-desorption curves. In Fig. 2c, the isotherm of obtained RGB-NMO is consistent with the type-IV character associated with H3 of the hysteresis loop, illustrating the formation of typical mesoporous structure by using CTAB-assisted strategy. Specifically, the specific surface area (SSA) of RGB-NMO is 40.6 $\text{m}^2 \text{g}^{-1}$, which is much

higher than that of LGB-NMO (9.9 $\text{m}^2 \text{g}^{-1}$). It is known that the larger SSA cannot only increase the exposure of active sites, but also provide more channels for the adsorption and desorption process in catalysis [49]. As shown in Fig. 2d, the CTAB-assisted synthesis strategy can also increase the pore volume from 0.01 to 0.07 $\text{cm}^3 \text{g}^{-1}$. The superior porosity of RGB-NMO relative to LGB-NMO can further engineer the structural advantage to accelerate the mass transfer during ODS procedure, which is conducive to the DBT catalytic oxidation process [50].

To further analyze the surface chemical composition and the fine structure difference, X-ray photoelectron spectra (XPS) were performed on as-prepared samples. As shown in Fig. S3, the survey XPS spectra illustrate the coexistence of Ni, Mo and O elements in the materials. Based on the Mo 3d spectra in Fig. 3a, due to the addition of CTAB, the characteristic peak of Mo 3d_{5/2} (232.2 eV) and Mo 3d_{3/2} (235.3 eV) both shift 0.1 eV to lower binding energy, corresponding to Mo⁶⁺ [51]. As shown in Fig. 3b, the Ni 2p spectra of the as-prepared catalysts are deconvoluted into two pairs of fitting peaks. Note that the ratio of Ni³⁺ in RGB-NMO (31.1%) is less than that of LGB-NMO (40.1%) [52], reflecting that CTAB-assisted strategy may increase the oxygen vacancies. Three fitted peaks located at 530.5, 531.1 and 533.1 eV are observed in the XPS O 1s region (Fig. 3c), which are ascribed to lattice oxygen (O_L), oxygen vacancy (O_V) and surface oxygen (O_S), respectively [53,54]. It is worthy noticing that the proportion of O_V is 32.3% in RGB-NMO, whereas only 21.1% is observed in LGB-NMO, which may be due to the restructured distorted area and more interface defects in RGB-NMO after GB engineering. In addition, the O_V concentration in RGB-NMO and LGB-NMO is further determined by electron paramagnetic resonance (EPR). As depicted in Fig. 3d, a stronger ESR signal identified at g = 2.003 is detected in RGB-NMO, illustrating that more oxygen vacancies have been formed in RGB-NMO than in LGB-NMO through GB engineering, which is consistent with the results of XPS analysis [55].

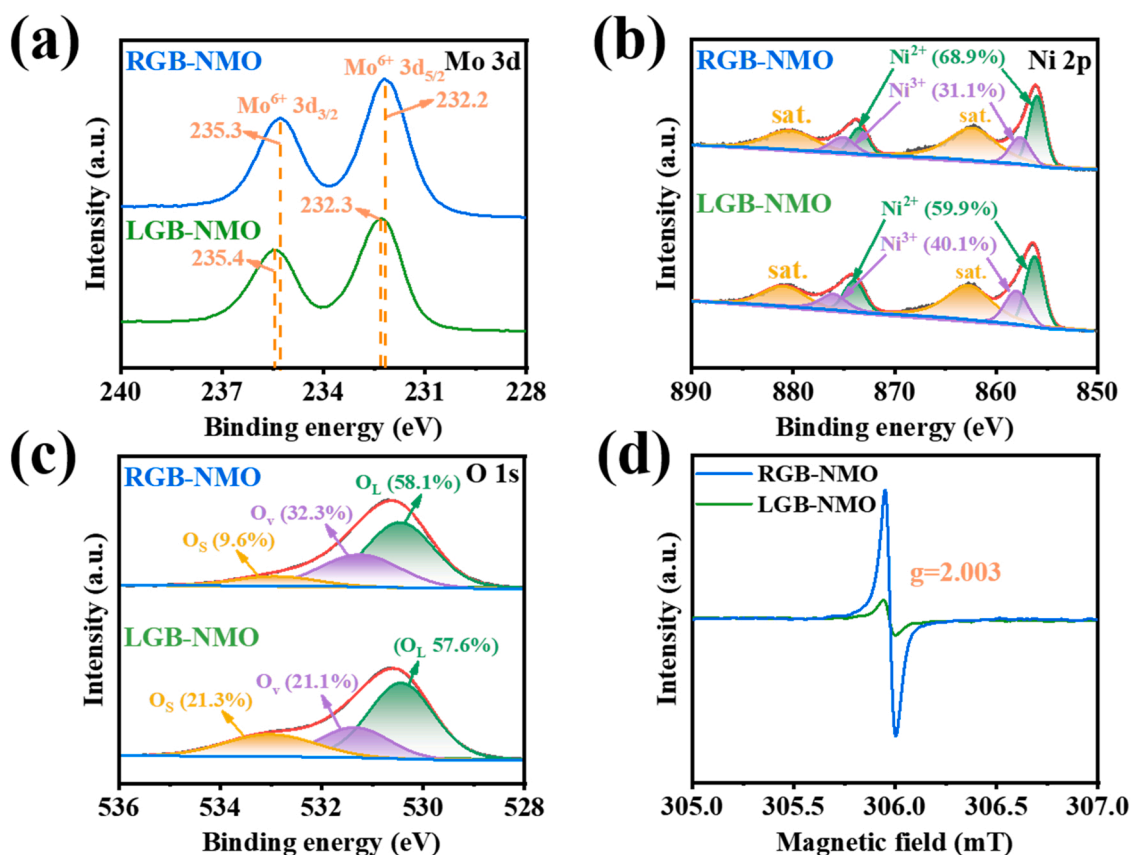


Fig. 3. High resolution of (a) Mo 3d, (b) Ni 2p, (c) O 1s XPS spectra and (d) EPR spectra of LGB-NMO and RGB-NMO.

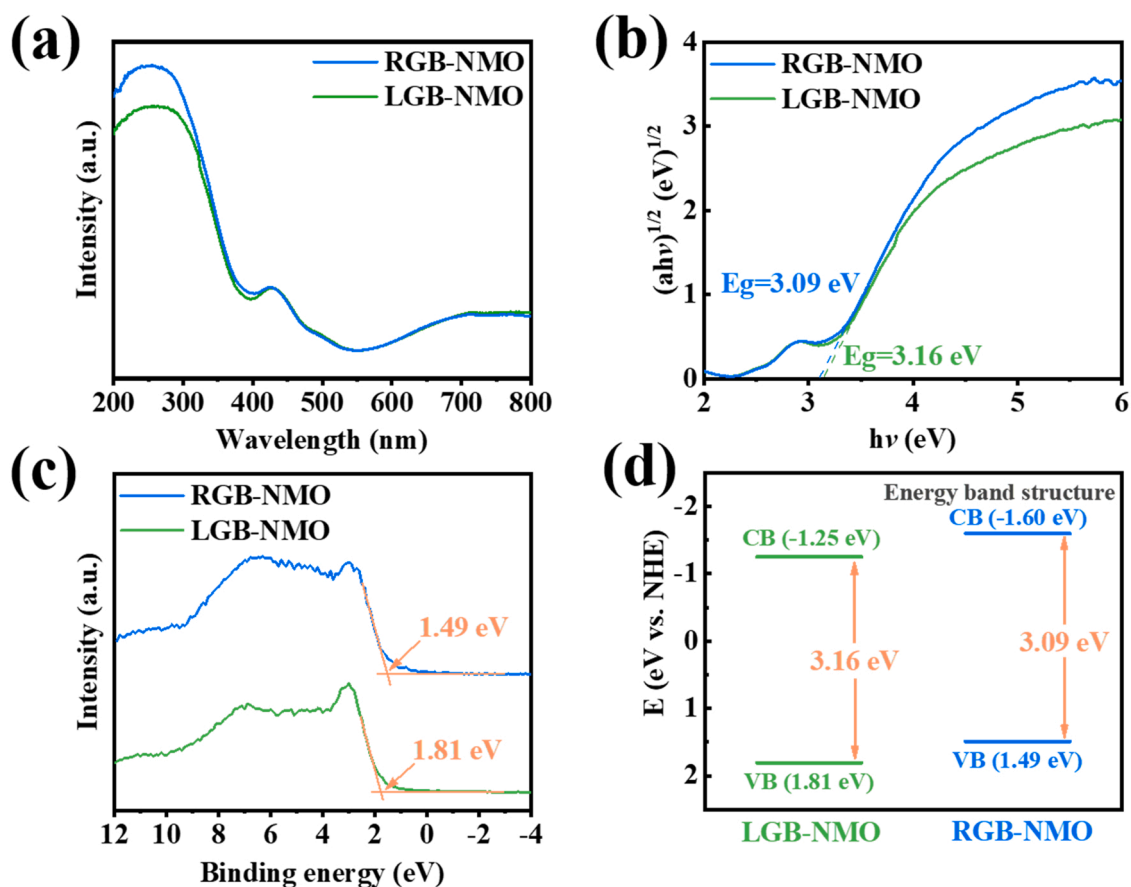


Fig. 4. (a) UV-vis DRS of the prepared samples. (b) The corresponding Kubelka-Munk plots. (c) Valence band XPS spectra and (d) proposed band structures of LGB-NMO and RGB-NMO samples.

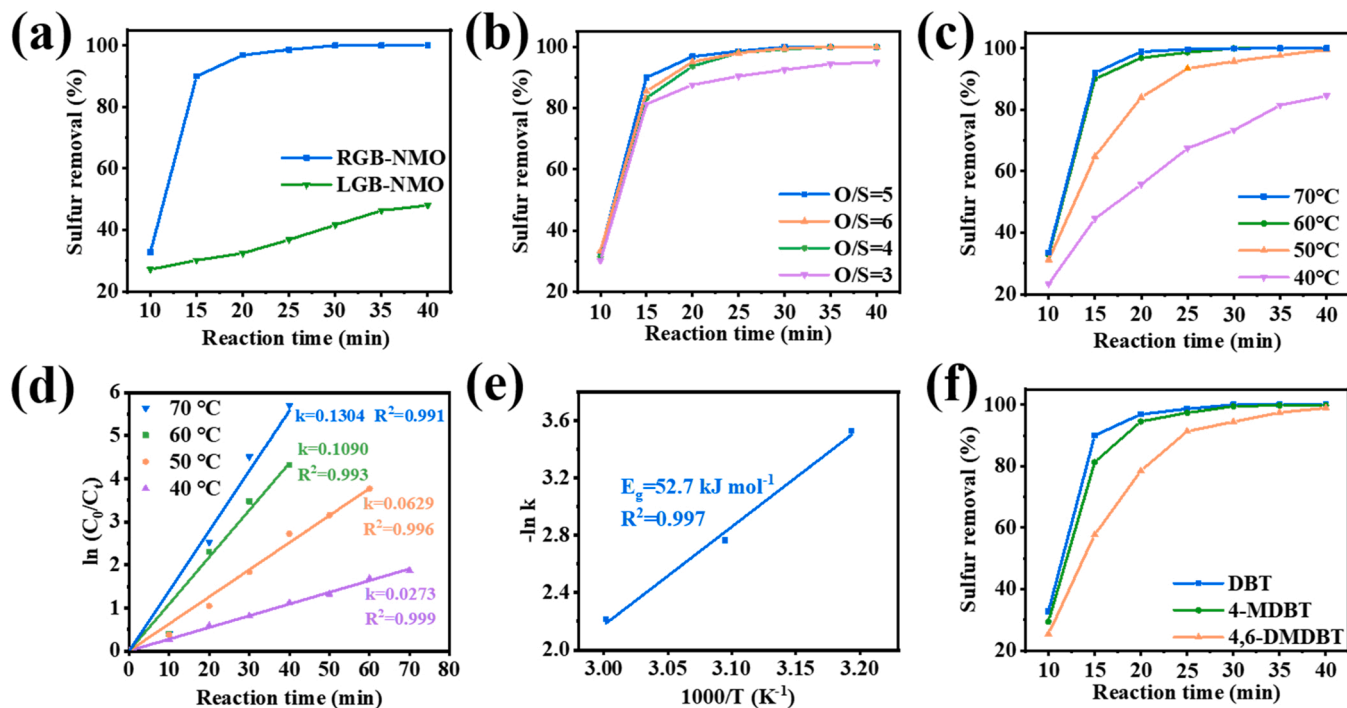


Fig. 5. Catalytic ODS activity (a) with various catalysts; (b) with various ratios of O/S; (c) at different reaction temperatures. (d) Pseudo first-order kinetics and (e) Arrhenius plots for DBT oxidation at the different temperatures. (f) Catalytic ODS activity for different sulfur-containing substances. Optimal experimental conditions: m (catalyst) = 20 mg, V (model oil) = 5 mL, V ([OMIM]BF₄) = 1 mL, O/S = 5, T = 60 °C.

The UV-vis diffuse reflection spectra (UV-vis DRS) of obtained catalysts were shown in Fig. 4a. As is known that more oxygen vacancies can lead to the enhanced visible light adsorption in RGB-NMO compared with LGB-NMO, causing by the formed transition of sub-band states at the defect energy levels [56]. The increased concentration of oxygen vacancies cannot only greatly modulate the electronic compositions, but also produce a favorable surrounding to accelerate the ODS procedure [57]. Moreover, it is observed that the bandgap energies of LGB-NMO and RGB-NMO are 3.16 and 3.09 eV based on the corresponding Kubelka-Munk plots (Fig. 4b). Combined with the XPS valence band (VB) spectra (Fig. 4c), the conduction bands (CB) were estimated to be -1.25 and -1.60 eV for LGB-NMO and RGB-NMO, respectively (Fig. 4d) [58]. Upon gathering the above analysis, it is concluded that GB engineering can narrow the bandgap and lower the CB situation of RGB-NMO, leading to the formation of more high-energy electrons, which is beneficial to the activation of H_2O_2 to yield hydroxyl radical [57,59].

3.2. Evaluation of ODS performance

The prepared catalysts were added into a dodecane/[OMIM]BF₄ biphasic system with the existence of H_2O_2 as the oxidant to evaluate their catalytic desulfurization abilities via ODS reaction. [OMIM]BF₄, a polar extractant, was introduced into the reaction system to make the catalysts, oxidants and reactants contact closely. The extraction equilibrium could be achieved after 10 min of extraction. Following that, a certain amount of H_2O_2 was added into the reaction system. It is observed that RGB-NMO shows greatly improved catalytic ODS activity than LGB-NMO (Fig. 5a). Specifically, RGB-NMO exhibits a marvelous catalytic activity of 100% removal efficiency within 30 min, while only 41.6% DBT can be removed by LGB-NMO under the identical condition, which reveals the advantages of CTAB-assisted synthesis strategy. As shown in Table S2, compared with several representative metal oxide catalysts in ODS, RGB-NMO is a promising catalyst by which refractory sulfides can be completely removed within 30 min under mild reaction conditions ($T = 60^\circ\text{C}$, $\text{O/S} = 5$) to produce ultraclean fuels, which leaps to the front ranks of the reported other similar catalysts [19,60–67].

Additionally, to further determine the effect of CTAB amount on textural properties of catalysts, a series of samples were prepared by adding various concentrations of CTAB (2.5, 5, 7.5 and 10 g/L), and SEM (Fig. S4), XRD (Fig. S5), FT-IR (Fig. S6), Raman (Fig. S7) and N_2 adsorption-desorption analyses (Fig. S8) were carried out. These analyses illustrate that the pore distributions, crystal structures and chemical compositions of as-prepared catalysts are greatly affected by the amount of CTAB. Notably, among them, RGB-NMO synthesized with 7.5 g/L CTAB exhibits the preferred mixed crystal structure and the best porosity. Combined with their catalytic tests (Fig. S9), the CTAB-assisted strategy is of great importance to improve the catalytic activity through engineering GB and optimizing its morphology. Moreover, compared with the systems containing various squaternary ammonium salts with a shorter alkyl chain (TTAB, DTAB and TMAB), RGB-NMO features the best catalytic ODS activity (Fig. S10). The corresponding XRD analysis are shown in Fig. S11, it is observed that the mixed crystalline phase cannot be generated when DTAB and TMAB are introduced into reaction system, which indicates that the alkyl chain of quaternary ammonium salts also has a great impact on the formation of catalysts rich in GB. Besides, considering their similar SSA and pore distributions (Fig. S12 and Table S3), the enhanced catalytic performance of RGB-NMO is undoubtedly caused by the unique plentiful GB as active centers.

The H_2O_2 /sulfur (O/S) molar ratio as a controlling factor of ODS was investigated with RGB-NMO as the catalyst. As illustrated in Fig. 5b, the catalytic activity of RGB-NMO is gradually enhanced with the increase in molar ratio of O/S (from 3 to 5), further implying that the oxidant has a great contribution to the ODS process. However, a slight loss of sulfur removal of DBT was observed as the molar O/S ratio was further increased to 6. This phenomenon may be attributed to the fact that more

water induced by the excessive H_2O_2 into the reaction system not only inhibits the mass transfer, but also dilutes the concentration of [OMIM]BF₄ and then decreases the solubility of DBT in the extraction phase. Generally, as a typical endothermal reaction, ODS process benefits from high reaction temperature. In Fig. 5c, a greatly enhanced catalytic activity was observed with the temperature varying from 40° to 60°C . Particularly, the sulfur removal of DBT can only reach 84.5% within 40 min when the temperature is 40°C . As the temperature is increased to 50°C , DBT can be completely removed after 40 min reaction. Significantly, further increasing temperature up to 60°C could shorten the time to 30 min to achieve complete desulfurization. Although the catalytic activity is still improved slightly as the temperature is further increased to 70°C , the self-decomposition of partial H_2O_2 and economic point of view should be taken into consideration. Hence, 60°C is the best choice for the ODS process. To better explain the oxidation reaction of DBT, the reaction kinetics as the primary parameter were calculated. As presented in Fig. 5, the studied ODS system displays a linear relationship between time and $\ln(C_0/C_t)$, which is well fitted the pseudo-first-order kinetic model. Notably, as the reaction temperature increases from 40 to 70°C , the reaction rate constants of DBT increases from 0.0273 to 0.1304 min^{-1} , further proving that high reaction temperature is beneficial to ODS reaction. Moreover, according to the linear relationship between $1000/T$ and $-\ln k$, the activation energy (E_a) for the DBT was found to be 52.7 kJ mol^{-1} (Fig. 5e).

The chemical environment and composition of sulfur atom has an effect on the ODS activity. Therefore, different aromatic sulfur-containing compounds (DBT, 4-MDBT and 4,6-DMDBT) as representative substrates were selected to be investigated. As shown in Fig. 5f, ultra-deep desulfurization could be achieved for all substrates under identical reaction conditions. In particular, the sequence of desulfurization efficiency was $\text{DBT} > 4\text{-MDBT} > 4,6\text{-DMDBT}$, which may be affected by the steric hindrance of the sulfur atom [68]. In general, the accessibility of S atoms of 4,6-DMDBT and 4-MDBT is decreased relative to DBT, leading to a lower catalytic oxidation activity due to a stronger spatial site resistance effect of the methyl group. Furthermore, aromatics and olefins, as typical interfering substances in the actual diesel, exert great influence on ODS process. Herein, toluene and 1-octene as aromatics and olefins representative interferences, respectively, with the concentration of 10 wt% (the mass percentage in model oil) were added into the reaction solution to explore their effects on the desulfurization activity. It is observed that DBT is completely removed with the addition of toluene, inflecting that the catalytic activity of RGB-NMO is almost unaffected by toluene (Fig. S13). Whereas, the sulfur removal is slightly decreased to 95.6% after 40 min reaction when 1-octene was added into the reaction system. Therefore, it is concluded that the obtained RGB-NMO catalyst exhibits the potential practical application value in treating the actual fuels.

To further validate the reusability and stability of the catalyst, the used RGB-NMO catalyst was separated from the reaction system. After that, it is dried at 60°C overnight for the next cycle test. As shown in Fig. 6a, the sulfur removal capacity could still remain 96.9% at the fourteenth recycling. Whereas, the catalytic activity is slightly decreased to 87.5% after 15 times of recycling, which may be due to the gradual coverage of active centers and pores blockage by the reaction product in the previous reaction. To prove this hypothesis, the used catalyst was regenerated by simple ethanol washing. It is worth noticing that a superior catalytic activity was observed over the regenerated catalyst, illustrating that the catalyst shows high stability against the complex reaction operating conditions. In addition, according to the hot filtration experiment results (Fig. 6b), the ODS process is completely restrained after removing the catalyst from the reaction system, indicating that no catalysts leaching was observed during the reaction.

3.3. Possible reaction mechanism of ODS process

Exploring the reaction mechanism is vital to understanding of ODS

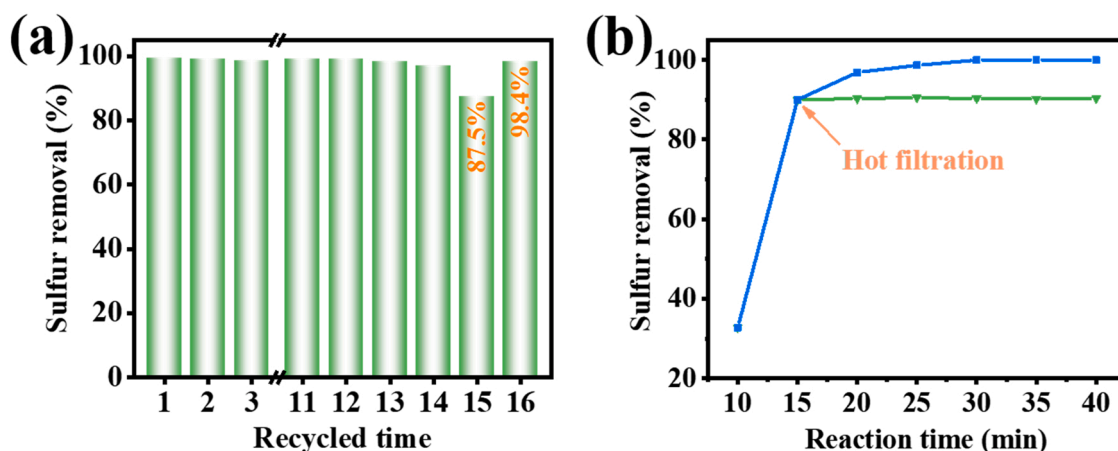


Fig. 6. (a) Recycling performance and (b) hot filtration test of RGB-NMO. Experimental conditions: m (catalyst) = 20 mg, V (model oil) = 5 mL, O/S = 5, T = 60 °C.

process and accurate design of catalysts. Free radical trap experiments were employed to determine the catalytic active intermediates during the reaction. In particular, dimethyl sulfoxide (DMSO), *p*-benzoquinone (BQ) and silver nitrate (AgNO_3) as the quenching agents, were added to the reaction system to quench hydroxyl radicals ($\bullet\text{OH}$), superoxide radicals ($\text{O}_2^{\bullet-}$) and electrons (e^-), respectively [69,70]. As shown in Fig. 7a, the addition of BQ has little impact on the ODS activity of the catalyst. Whereas, when DMSO was added into the reaction system, the desulfurization efficiency was significantly decreased to only 17.5% after reacting for 40 min. It can be deduced that $\bullet\text{OH}$ as the major catalytic active intermediate may be generated during the ODS process. Moreover, the experimental results also showed that the sulfur removal was almost completely inhibited by the introduction of AgNO_3 , illustrating the vital role of e^- during the ODS process. With the purpose of further confirming $\bullet\text{OH}$ is the main oxygen active species, electron spin resonance (ESR) spectroscopy was conducted with the presence of 5, 5-dimethyl-1-pyrrolin-N-oxide (DMPO) as the spin trap reagent [71]. As shown in Fig. 7b, no ESR signal was detected in the absence of H_2O_2 , and the stronger intensity of observed four-fold peak signal corresponding to $\bullet\text{OH}$ was generated over RGB-NMO compared with LGB-NMO. These results certainly reflect that grain boundary engineering is beneficial to the activation of H_2O_2 to obtain the active $\bullet\text{OH}$ species, matches with the results of free radical trap experiments.

To further explore the reaction process of ODS, the model oils of three time periods during the reaction procedure were analyzed by gas chromatography (GC) analysis (Fig. S14). It is known that the signal

peak located at 5.9 min is attributed to DBT [9]. Notably, the intensity of DBT peak kept decreasing as the reaction proceeded, and it completely disappeared after reacting for 30 min, inflecting that the DBT was completely removed from model oil via ODS reaction. Moreover, no new signal peaks ascribed to the oxidative products were detected in the model oil after reaction, which provided an evidence that the corresponding oxidation products were still retained in the extractant phase due to its high solubility [19]. With the purpose of determining the type of ODS products, the catalyst phase was collected and characterized by FT-IR analysis. As shown in Fig. S15, compared with the pristine catalyst, the new peak located at 1167 cm^{-1} is assigned to DBT sulfone (DBTO_2) [67]. The oxidative product can be also detected by XRD analysis, which matches well with the result of FT-IR (Fig. S16). The aforementioned experimental results suggest that DBT was oxidized to DBTO_2 via ODS reaction, which were accumulated in extractant phase and on the surface of the catalyst.

According to the above analysis combined with reported research studies, a possible mechanism is proposed to expound how the RGB-NMO works in the ODS process (Scheme 1). Sulfur-containing compounds are removed from the oil through two steps of extraction and oxidation in a desulfurization system, which is composed of two phases including nonpolar dodecane and polar $[\text{OMIM}]\text{BF}_4$. The different electronegativities between the Ni and Mo species can modulate the electron composition of reactive sites, enhancing the formation of electron rich Mo atoms, which leads to the higher electron-donating tendency. Moreover, through GB engineering, more energetic

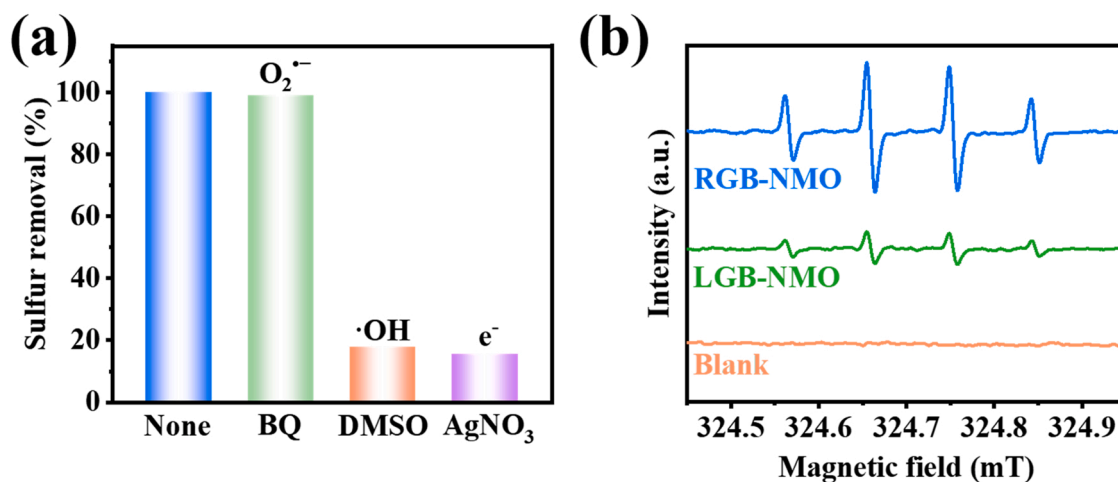
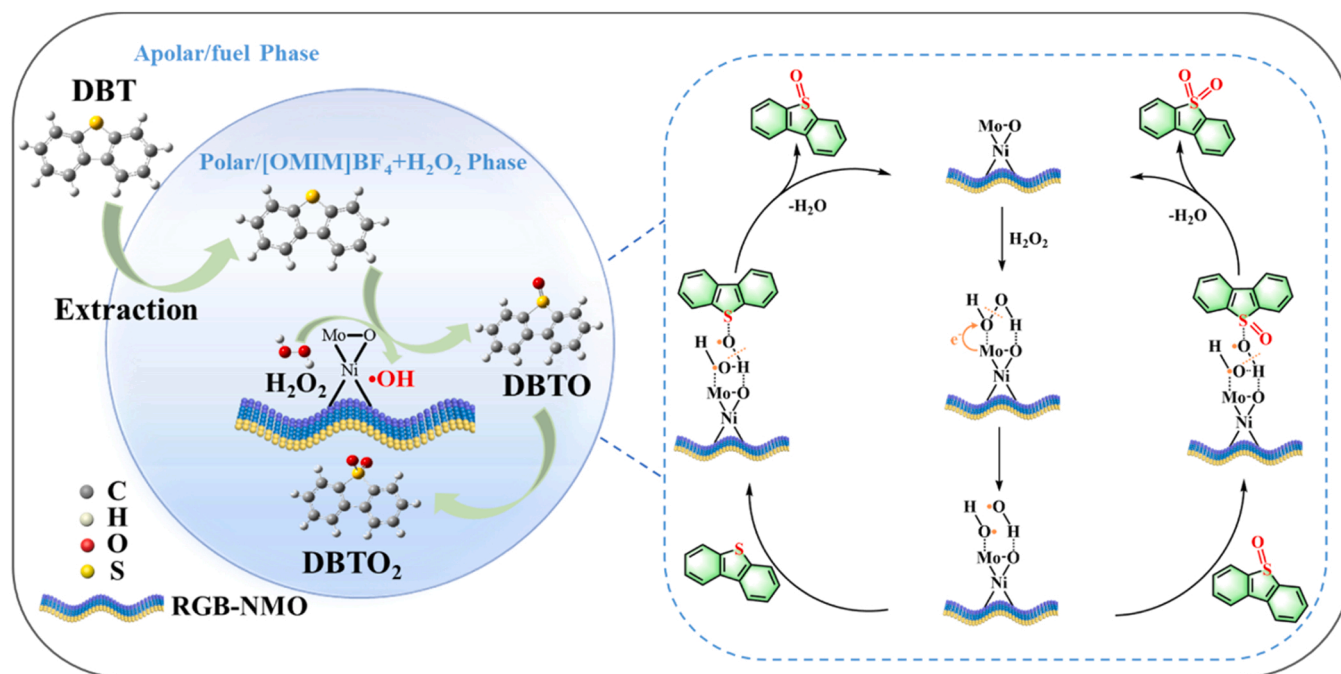


Fig. 7. (a) Effect of radical scavengers on the ODS efficiency of RGB-NMO. (b) ESR spectra with DMPO as the spin-trapping of as-prepared samples. Experimental conditions: m (catalyst) = 20 mg, V (model oil) = 5 mL, V ($[\text{OMIM}]\text{BF}_4$) = 1 mL, O/S = 5, T = 60 °C.



Scheme 1. Proposed reaction mechanism of ODS over RGB-NMO.

electrons were generated in RGB-NMO based on oxygen vacancies, facilitating the H_2O_2 -to-active $\bullet\text{OH}$ transformation. In the ODS process, DBT is firstly extracted into [OMIM] BF_4 phase diffused with H_2O_2 and RGB-NMO, which is beneficial to the full contact of DBT, H_2O_2 and active centers. Subsequently, the peroxy O atom of H_2O_2 is chemically absorbed onto the electron rich Mo atoms to yield a Mo-O-O-H-O five-member ring [72]. Following that, the O-O bonds break causing by the transfer of electrons from the Mo atoms with abundant electrons to the O atoms connected with them, thereby generating the active $\bullet\text{OH}$ radicals. This proposed reaction process is capable of providing direct evidence for the suppressed catalytic activity with AgNO_3 as the quenching agent, suggesting that the electron transfer plays a vital role during the ODS process. Eventually, the sulfur atom in DBT is attacked by the $\bullet\text{OH}$ with high oxidizing capability to produce DBTO, which is further converted to DBTO_2 as the ODS reaction proceeds. Meanwhile, the corresponding oxidation products are still retained in the extraction phase, leading to clean oil with ultralow sulfur content.

4. Conclusions

In summary, a CTAB-assisted strategy is employed to engineer GB into NiMoO_4 . For RGB-NMO, the constructed GB have been regarded as highly active reactive sites, which leads to much better catalytic activity compared with LGB-NMO. In addition, the obtained larger specific surface area is beneficial to the mass transfer and plays an important role in making active sites fully exposed. As a result, DBT can be completely removed from the model oil by RGB-NMO within 30 min, far better than that of 41.6% over LGB-NMO. Besides, the bonus of the GB engineering allows the RGB-NMO also displays a satisfactory reusability, in which the sulfur removal can still reach 96.9% after 14 cycles. This work may provide a new strategy to engineer GB into more functional materials for improving their catalytic performance.

CRediT authorship contribution statement

Xin An: Data curation, Formal analysis, Investigation, Writing – original draft, Writing – review & editing. **Wei Jiang:** Conceptualization, Funding acquisition, Project administration, Writing – review and

editing, Supervision. **Linhua Zhu:** Investigation, Funding acquisition. **Lingchao Xu:** Data curation, Methodology. **Junfeng She:** Data curation, Methodology. **Jing He:** Conceptualization, Formal analysis, Resources. **Wenshuai Zhu:** Conceptualization, Project administration, Supervision. **Huaming Li:** Project administration.

Declaration of Competing Interest

The authors declare that they have no known competing financial interests or personal relationships that could have appeared to influence the work reported in this paper.

Data Availability

No data was used for the research described in the article.

Acknowledgments

This work was financially supported by the National Natural Science Foundation of China (Nos. 21978119, 22078135, and 22202088), a Project Funded by the Priority Academic Program Development of Jiangsu Higher Education Institutions.

Appendix A. Supporting information

Supplementary data associated with this article can be found in the online version at [doi:10.1016/j.apcatb.2023.122779](https://doi.org/10.1016/j.apcatb.2023.122779).

References

- [1] S. Smolders, T. Willhammar, A. Krajnc, K. Sentosun, M.T. Wharmby, K. A. Lomachenko, S. Bals, G. Mali, M.B.J. Roeflaers, D.E. De Vos, B. Bueken, A titanium(IV)-Based metal-organic framework featuring defect-rich Ti-O sheets as an oxidative desulfurization catalyst, *Angew. Chem. Int. Ed.* 58 (2019) 9160–9165.
- [2] Y. Zhou, S. Yin, Y. Gao, Y. Zhao, M. Goto, L.-B. Han, Selective P-P and P-O-P bond formations through copper-catalyzed aerobic oxidative dehydrogenative couplings of H-Phosphonates, *Angew. Chem. Int. Ed.* 49 (2010) 6852–6855.
- [3] Z. Zhu, H. Ma, W. Liao, P. Tang, K. Yang, T. Su, W. Ren, H. Lu, Insight into tri-coordinated aluminum dependent catalytic properties of dealuminated Y zeolites in oxidative desulfurization, *Appl. Catal. B* 288 (2021), 120022.

- [4] A. Nisar, J. Zhuang, X. Wang, Construction of amphiphilic polyoxometalate mesostructures as a highly efficient desulfurization catalyst, *Adv. Mater.* 23 (2011) 1130–1135.
- [5] F. Lin, Z. Jiang, N. Tang, C. Zhang, Z. Chen, T. Liu, B. Dong, Photocatalytic oxidation of thiophene on $\text{RuO}_2/\text{SO}_4^{2-}\text{-TiO}_2$: Insights for cocatalyst and solid-acid, *Appl. Catal. B* 188 (2016) 253–258.
- [6] W. Jiang, H. Jia, H. Li, L. Zhu, R. Tao, W. Zhu, H. Li, S. Dai, Boric acid-based ternary deep eutectic solvent for extraction and oxidative desulfurization of diesel fuel, *Green Chem.* 21 (2019) 3074–3080.
- [7] L. Zhang, J. Wang, Y. Sun, B. Jiang, H. Yang, Deep oxidative desulfurization of fuels by superbase-derived Lewis acidic ionic liquids, *Chem. Eng. J.* 328 (2017) 445–453.
- [8] W. Jiang, K. Zhu, H. Li, L. Zhu, M. Hua, J. Xiao, C. Wang, Z. Yang, G. Chen, W. Zhu, H. Li, S. Dai, Synergistic effect of dual Brønsted acidic deep eutectic solvents for oxidative desulfurization of diesel fuel, *Chem. Eng. J.* 394 (2020), 124831.
- [9] X. An, L. Zhu, J. Xiao, W. Jiang, X. Gao, L. Xu, H. Li, W. Zhu, H. Li, Engineering hollow mesoporous silica supported cobalt molybdate catalyst by dissolution-regrowth strategy for efficiently aerobic oxidative desulfurization, *Fuel* 325 (2022), 124755.
- [10] G. Junzhen, C. Liang, Y. Haibin, H. Zhi, Y. Mu, W. Ge, Amphiphilic halloysite nanotube enclosing molybdenum oxide as nanoreactor for efficient desulfurization of model fuels, *Chem. Eng. J.* 451 (2022), 138595.
- [11] L. Sun, T. Su, J. Xu, D. Hao, W. Liao, Y. Zhao, W. Ren, C. Deng, H. Lü, Aerobic oxidative desulfurization coupling of Co polyanion catalysts and p-TsOH-based deep eutectic solvents through a biomimetic approach, *Green Chem.* 21 (2019) 2629–2634.
- [12] F. Liu, J. Yu, A.B. Qazi, L. Zhang, X. Liu, Metal-Based ionic liquids in oxidative desulfurization: a critical review, *Environ. Sci. Technol.* 55 (2021) 1419–1435.
- [13] Z. Zhu, H. Ma, W. Liao, P. Tang, K. Yang, T. Su, W. Ren, H. Lü, Insight into tri-coordinated aluminum dependent catalytic properties of dealuminated Y zeolites in oxidative desulfurization, *Appl. Catal. B* 288 (2021), 120022.
- [14] J. He, P. Wu, L. Chen, H. Li, M. Hua, L. Lu, Y. Wei, Y. Chao, S. Zhou, W. Zhu, H. Li, Dynamically-generated TiO_2 active site on MXene Ti_3C_2 : Boosting reactive desulfurization, *Chem. Eng. J.* 416 (2021), 129022.
- [15] S. Wei, H. He, Y. Cheng, C. Yang, G. Zeng, L. Kang, H. Qian, C. Zhu, Preparation, characterization, and catalytic performances of cobalt catalysts supported on KIT-6 silicas in oxidative desulfurization of dibenzothiophene, *Fuel* 200 (2017) 11–21.
- [16] W. Jiang, J. Xiao, X. Gao, X. An, Y. Leng, L. Zhu, W. Zhu, H. Li, In situ fabrication of hollow silica confined defective molybdenum oxide for enhanced catalytic oxidative desulfurization of diesel fuels, *Fuel* 305 (2021), 121470.
- [17] X. Liao, Y. Huang, Y. Zhou, H. Liu, Y. Cai, S. Lu, Y. Yao, Homogeneously dispersed HPW/graphene for high efficient catalytic oxidative desulfurization prepared by electrochemical deposition, *Appl. Surf. Sci.* 484 (2019) 917–924.
- [18] P. Wang, L. Jiang, X. Zou, H. Tan, P. Zhang, J. Li, B. Liu, G. Zhu, Confining polyoxometalate clusters into porous aromatic framework materials for catalytic desulfurization of dibenzothiophene, *ACS Appl. Mater. Mater.* 12 (2020) 25910–25919.
- [19] H. Wang, M. Tang, F. Shi, R. Ding, L. Wang, J. Wu, X. Li, Z. Liu, B. Lv, Amorphous Cr_2WO_6 -Modified WO_3 nanowires with a large specific surface area and rich Lewis acid sites: a highly efficient catalyst for oxidative desulfurization, *ACS Appl. Mater. Inter.* 12 (2020) 38140–38152.
- [20] W. Jiang, X. An, J. Xiao, Z. Yang, J. Liu, H. Chen, H. Li, W. Zhu, H. Li, S. Dai, Enhanced oxygen activation achieved by robust single chromium atom-derived catalysts in aerobic oxidative desulfurization, *ACS Catal.* 12 (2022) 8623–8631.
- [21] J. He, S. Zhou, P. Wu, Y. Wu, L. He, L. Zhu, W. Zhu, H. Li, Multi-walled carbon nanotubes coated on defective tungsten oxide for deep oxidative desulfurization of diesel fuels, *Fuel Process. Technol.* 236 (2022), 107399.
- [22] C. Yuan, J. Li, L. Hou, X. Zhang, L. Shen, X.W. Lou, Ultrathin mesoporous NiCo_2O_4 nanosheets supported on Ni foam as advanced electrodes for supercapacitors, *Adv. Funct. Mater.* 22 (2012) 4592–4597.
- [23] D. Guo, H. Zhang, X. Yu, M. Zhang, P. Zhang, Q. Li, T. Wang, Facile synthesis and excellent electrochemical properties of CoMoO_4 nanoplate arrays as supercapacitors, *J. Mater. Chem. A* 1 (2013) 7247–7254.
- [24] S. Huang, P. Xin, C. Wu, S. Fei, Q. Zhang, Y. Jiang, Z. Chen, L. Selegard, K. Uvdal, Z. Hu, Fabrication of multi-layer CoSnO_3 @carbon-caged NiCo_2O_4 nanobox for enhanced lithium storage performance, *Chem. Eng. J.* 410 (2021), 128458.
- [25] T. Xiong, B. Huang, J. Wei, X. Yao, R. Xiao, Z. Zhu, F. Yang, Y. Huang, H. Yang, M.-S.J.T. Balogun, Unveiling the promotion of accelerated water dissociation kinetics on the hydrogen evolution catalysis of NiMoO_4 nanorods, *J. Energy Chem.* 67 (2021) 805–813.
- [26] Z. Zhang, H. Zhang, X. Zhang, D. Yu, Y. Ji, Q. Sun, Y. Wang, X. Liu, Facile synthesis of hierarchical CoMoO_4 @ NiMoO_4 core-shell nanosheet arrays on nickel foam as an advanced electrode for asymmetric supercapacitors, *J. Mater. Chem. A* 4 (2016) 18578–18584.
- [27] S. Pratiya, S. Manickam Minakshi, W. Teeraphat, W.L. Damian, E. Holger, A. Rajeev, Zn metal atom doping on the surface plane of 1D NiMoO_4 nanorods with improved redox chemistry, *ACS Appl. Mater. Inter.* 12 (2020) 44815–44829.
- [28] Y. Zeng, J. Liao, B. Wei, Z. Huang, W. Zhu, J. Zheng, H. Liang, Y. Zhang, Z. Wang, Tuning the electronic structure of NiMoO_4 by coupling with SnO_2 for high-performance hybrid supercapacitors, *Chem. Eng. J.* 409 (2020), 128297.
- [29] J. He, N. Li, Z.G. Li, M. Zhong, Z.X. Fu, M. Liu, J.C. Yin, Z. Shen, W. Li, J. Zhang, Z. Chang, X.H. Bu, Strategic defect engineering of metal-organic frameworks for optimizing the fabrication of single-atom catalysts, *Adv. Funct. Mater.* 31 (2021) 2103597.
- [30] R. Yang, S. Peng, B. Lan, M. Sun, Z. Zhou, C. Sun, Z. Gao, G. Xing, L. Yu, Oxygen defect engineering of $\beta\text{-MnO}_2$ catalysts via phase transformation for selective catalytic reduction of NO, *Small* 17 (2021) 2102408.
- [31] J. Di, C. Yan, A.D. Handoko, Z.W. Seh, H. Li, Z. Liu, Ultrathin two-dimensional materials for photo- and electrocatalytic hydrogen evolution, *Mater. Today* 21 (2018) 749–790.
- [32] R. Shen, Y. Liu, H. Wen, T. Liu, Z. Peng, X. Wu, X. Ge, S. Mehdi, H. Cao, E. Liang, J. Jiang, B. Li, Engineering V_2O_5 -Ti ensemble to boost the activity of Ru towards water dissociation for catalytic hydrogen generation, *Appl. Catal. B* 306 (2022), 121100.
- [33] X. Ma, M. Xiao, X. Yang, X. Yu, M. Ge, Boosting benzene combustion by engineering oxygen vacancy-mediated $\text{Ag/CeO}_2\text{-Co}_3\text{O}_4$ catalyst via interfacial electron transfer, *J. Colloid Interf. Sci.* 594 (2021) 882–890.
- [34] J. Di, J. Xiong, H. Li, Z. Liu, Ultrathin 2D photocatalysts: electronic-structure tailoring, hybridization, and applications, *Adv. Mater.* 30 (2018) 1704740.
- [35] R. Shi, Y. Zhao, G.I.N. Waterhouse, S. Zhang, T. Zhang, Defect engineering in photocatalytic nitrogen fixation, *ACS Catal.* 9 (2019) 9739–9750.
- [36] H. Huang, H. Jung, H. Jun, D.Y. Woo, J.W. Han, J. Lee, Design of grain boundary enriched bimetallic borides for enhanced hydrogen evolution reaction, *Chem. Eng. J.* 405 (2020), 126977.
- [37] Y. He, P. Tang, Z. Hu, Q. He, C. Zhu, L. Wang, Q. Zeng, P. Golani, G. Gao, W. Fu, Z. Huang, C. Gao, J. Xia, X. Wang, X. Wang, C. Zhu, Q.M. Ramasse, A. Zhang, B. An, Y. Zhang, S. Martí-Sánchez, J.R. Morante, L. Wang, B.K. Tay, B.I. Yakobson, A. Trampert, H. Zhang, M. Wu, Q.J. Wang, J. Arbiol, Z. Liu, Engineering grain boundaries at the 2D limit for the hydrogen evolution reaction, *Nat. Commun.* 11 (2020) 57.
- [38] Y. Chen, Y. Wang, J. Yu, G. Xiong, H. Niu, Y. Li, D. Sun, X. Zhang, H. Liu, W. Zhou, Underflow laser induced ni nanoparticles embedded metallic mon microrods as patterned electrode for efficient overall water splitting, *Adv. Sci.* 9 (2022) 2105869.
- [39] K. Hu, S. Jeong, G. Elumalai, S. Kukunuri, J.-i Fujita, Y. Ito, Phase-Dependent reactivity of nickel molybdates for electrocatalytic urea oxidation, *ACS Appl. Energy Mater.* 3 (2020) 7535–7542.
- [40] Z. Yao, G. Haoran, L. Xinpan, R. Wenlu, S. Rui, The synergetic effect of the mixed phase of NiMoO_4 with a 1D–2D–3D hierarchical structure for a highly efficient and stable urea oxidation reaction, *Mater. Chem. Front.* 6 (2022) 1477–1486.
- [41] K. Jing, W. Ma, Y. Ren, J. Xiong, B. Guo, Y. Song, S. Liang, L. Wu, Hierarchical Bi_2MoO_6 spheres in situ assembled by monolayer nanosheets toward photocatalytic selective oxidation of benzyl alcohol, *Appl. Catal. B* 243 (2018) 10–18.
- [42] Z. Chen, N. Mi, L. Huang, W. Wang, C. Li, Y. Teng, C. Gu, Snow-like BiVO_4 with rich oxygen defects for efficient visible light photocatalytic degradation of ciprofloxacin, *Sci. Total Environ.* 808 (2021), 152083.
- [43] X. Fan, J. Li, Z. Zhao, Y. Wei, J. Liu, A. Duan, G. Jiang, Synthesis of a new ordered mesoporous NiMoO_4 complex oxide and its efficient catalytic performance for oxidative dehydrogenation of propane, *J. Energy Chem.* 23 (2014) 171–178.
- [44] X. Lu, W. Jia, H. Chai, J. Hu, S. Wang, Y. Cao, Solid-state chemical fabrication of one-dimensional mesoporous β -nickel molybdate nanorods as remarkable electrode material for supercapacitors, *J. Colloid Interf. Sci.* 534 (2018) 322–331.
- [45] J. Yuan, D. Yao, L. Jiang, Y. Tao, J. Che, G. He, H. Chen, Mn-Doped NiMoO_4 mesoporous nanorods/reduced graphene oxide composite for high-performance all-solid-state supercapacitor, *ACS Appl. Energy Mater.* 3 (2020) 1794–1803.
- [46] G. Kianpour, M. Salavati-Niasari, H. Emadi, Sonochemical synthesis and characterization of NiMoO_4 nanorods, *Ultrason. Sonochem.* 20 (2012) 418–424.
- [47] Y. Li, S. Zhang, M. Ma, X. Mu, Y. Zhang, J. Du, Q. Hu, B. Huang, X. Hua, G. Liu, E. Xie, Z. Zhang, Manganese-doped nickel molybdate nanostructures for high-performance asymmetric supercapacitors, *Chem. Eng. J.* 372 (2019) 452–461.
- [48] A. Rajput, M.K. Adak, B. Chakraborty, Intrinsic Lability of NiMoO_4 to excel the oxygen evolution reaction, *Inorg. Chem.* 61 (2022) 11189–11206.
- [49] Y. Zhao, Q. Tang, B. He, P. Yang, Mo incorporated $\text{W}_{18}\text{O}_{49}$ nanofibers as robust electrocatalysts for high-efficiency hydrogen evolution, *Int. J. Hydrog. Energ.* 42 (2017) 14534–14546.
- [50] J. Xiong, J. Li, H. Huang, M. Zhang, W. Zhu, J. Zhou, H. Li, J. Di, Electronic state tuning over Mo-doped $\text{W}_{18}\text{O}_{49}$ ultrathin nanowires with enhanced molecular oxygen activation for desulfurization, *Sep. Purif. Technol.* 294 (2022), 121167.
- [51] M. Pang, S. Jiang, Y. Ji, J. Zhao, B. Xing, Q. Pan, H. Yang, W. Qu, L. Gu, H. Wang, Comparison of alpha- NiMoO_4 nanorods and hierarchical alpha- NiMoO_4 @delta- MnO_2 core-shell hybrid nanorod/nanosheet aligned on Ni foam for supercapacitors, *J. Alloy. Compd.* 708 (2017) 14–22.
- [52] C. Ye, J. Liu, Q. Zhang, X. Jin, Y. Zhao, Z. Pan, G. Chen, Y. Qiu, D. Ye, L. Gu, G.I. N. Waterhouse, L. Guo, S. Yang, Activating metal oxides nanocatalysts for electrocatalytic water oxidation by quenching-induced near-surface metal atom functionality, *J. Am. Chem. Soc.* 143 (2021) 14169–14177.
- [53] H. Liang, J. Lin, H. Jia, S. Chen, J. Qi, J. Cao, T. Lin, W. Fei, J. Feng, Hierarchical NiCo-LDH @ NiOOH core-shell heterostructure on carbon fiber cloth as battery-like electrode for supercapacitor, *J. Power Sources* 378 (2018) 248–254.
- [54] J. Zou, Y. Lin, S. Wu, Y. Zhong, C. Yang, Molybdenum dioxide nanoparticles anchored on nitrogen-doped carbon nanotubes as oxidative desulfurization catalysts: role of electron transfer in activity and reusability, *Adv. Funct. Mater.* 31 (2021) 2100442.
- [55] J. Di, C. Chen, C. Zhu, R. Long, H. Chen, X. Cao, J. Xiong, Y. Weng, L. Song, S. Li, H. Li, Y. Xiong, Z. Liu, Surface local polarization induced by bismuth-oxygen vacancy pairs tuning non-covalent interaction for CO_2 photoreduction, *Adv. Energy Mater.* 11 (2021) 2102389.
- [56] J. Di, J. Xia, M.F. Chisholm, J. Zhong, C. Chen, X. Cao, F. Dong, Z. Chi, H. Chen, Y.-X. Weng, J. Xiong, S.-Z. Yang, H. Li, Z. Liu, S. Dai, Defect-Tailoring mediated

- electron-hole separation in single-unit-cell $\text{Bi}_3\text{O}_4\text{Br}$ nanosheets for boosting photocatalytic hydrogen evolution and nitrogen fixation, *Adv. Mater.* 31 (2019) 1807576.
- [57] J. Xiong, J. Li, C. Chen, W. Jiang, W. Zhu, H. Li, J. Di, Universal strategy engineering grain boundaries for catalytic oxidative desulfurization, *Appl. Catal. B* 317 (2022), 121714.
- [58] S. Lv, Y.H. Ng, R. Zhu, S. Li, C. Wu, Y. Liu, Y. Zhang, L. Jing, J. Deng, H. Dai, Phosphorus vapor assisted preparation of P-doped ultrathin hollow $\text{g-C}_3\text{N}_4$ sphere for efficient solar-to-hydrogen conversion, *Appl. Catal. B* 297 (2021), 120438.
- [59] J. Xiong, P. Song, J. Di, H. Li, Ultrathin structured photocatalysts: a versatile platform for CO_2 reduction, *Appl. Catal. B* 256 (2019), 117788.
- [60] M.A. Alvarez-Amparán, D. Guillén-Aguilar, L. Cedeño-Caero, MoWFe based catalysts to the oxidative desulfurization of refractory dibenzothiophene compounds: Fe promoting the catalytic performance, *Fuel Process. Technol.* 198 (2020), 106233.
- [61] F. Mohammad Hossein, M. Vahid, Novel synthesis of highly dispersed molybdenum oxide over nanorods cryptomelane octahedral manganese oxide molecular sieve ($\text{MoO}_3/\text{nanorod-OMS-2}$) as a high performance catalyst for oxidative desulfurization process, *Fuel Process. Technol.* 236 (2022), 107415.
- [62] M.A. Astle, G.A. Rance, H.J. Loughlin, T.D. Peters, A.N. Khlobystov, Molybdenum dioxide in carbon nanoreactors as a catalytic nanosponge for the efficient desulfurization of liquid fuels, *Adv. Funct. Mater.* 29 (2019) 1808092.
- [63] S. Hasannia, M. Kazemeini, A. Rashidi, A. Seif, The oxidative desulfurization process performed upon a model fuel utilizing modified molybdenum based nanocatalysts: experimental and density functional theory investigations under optimally prepared and operated conditions, *Appl. Surf. Sci.* 527 (2020), 146798.
- [64] M. Zuo, X. Huang, J. Li, Q. Chang, Y. Duan, L. Yan, Z. Xiao, S. Mei, S. Lu, Y. Yao, Oxidative desulfurization in diesel via a titanium dioxide triggered thermocatalytic mechanism, *Catal. Sci. Technol.* 9 (2019) 2923–2930.
- [65] J. Ye, J. Wen, D. Zhao, P. Zhang, A. Li, L. Zhang, H. Zhang, M. Wu, Macroporous 3D carbon-nitrogen (CN) confined MoO_x catalyst for enhanced oxidative desulfurization of dibenzothiophene, *Chin. Chem. Lett.* 31 (2020) 2819–2824.
- [66] J. He, P. Wu, Y. Wu, H. Li, W. Jiang, S. Xun, M. Zhang, W. Zhu, H. Li, Taming interfacial oxygen vacancies of amphiphilic tungsten oxide for enhanced catalysis in oxidative desulfurization, *ACS Sustain. Chem. Eng.* 5 (2017) 8930–8938.
- [67] Y. Cao, H. Wang, R. Ding, L. Wang, Z. Liu, B. Lv, Highly efficient oxidative desulfurization of dibenzothiophene using Ni modified MoO_3 catalyst, *Appl. Catal. A* 589 (2020), 117308.
- [68] X. An, W. Jiang, J. He, L. Zhu, L. Xu, H. Li, W. Zhu, H. Li, Modulating electronic characteristics of nickel molybdate via an effective manganese-doping strategy to enhance oxidative desulfurization performance, *Inorg. Chem.* 61 (2022) 21067–21075.
- [69] X. Wei, D. Xie, K. Yang, Z. Zhu, T. Su, W. Ren, C. Chen, Q. Zhang, H. Lü, Biomimetic catalytic aerobic oxidative desulfurization of diesel with NHPI-based ternary deep eutectic solvents, *Fuel Process. Technol.* 242 (2022), 107631.
- [70] X.-X. Xing, H.-L. Guo, T.-M. He, X. An, H.-P. Li, W.-S. Zhu, H.-M. Li, J.-Y. Pang, D.-B. Dang, Y. Bai, Tungstovanadate-based ionic liquid catalyst $[\text{C}_2(\text{MIM})_2]_2\text{VW}_{12}\text{O}_{40}$ used in deep desulfurization for ultraclean fuel with simultaneous recovery of the sulfone product, *ACS Sustain. Chem. Eng.* 10 (2022) 11533–11543.
- [71] Q. Huo, G. Liu, H. Sun, Y. Fu, Y. Ning, B. Zhang, X. Zhang, J. Gao, J. Miao, X. Zhang, S. Liu, CeO_2 -modified MIL-101(Fe) for photocatalysis extraction oxidation desulfurization of model oil under visible light irradiation, *Chem. Eng. J.* 422 (2021), 130036.
- [72] C. Lei, R. Jin-Tao, Y. Zhong-Yong, Identifying the dominant effect of electron-feeding on molybdenum phosphonates to decipher the activity origin for oxidative desulfurization of fuel, *Chem. Eng. J.* 450 (2022), 138330.